Monthly Notices of the ROYAL ASTRONOMICAL SOCIETY

MNRAS **478,** 4710–4719 (2018) doi:10.1093/mnras/sty1142

Superhump period of the black hole X-ray binary GX 339−4

Ilia A. Kosenkov[1,2]★ and Alexandra Veledina[1,3,4]★

[1]*Department of Physics and Astronomy, FI-20014 University of Turku, Finland*
[2]*Department of Astrophysics, St Petersburg State University, Universitetskiy Pr. 28, Peterhof, 198504 St Petersburg, Russia*
[3]*Nordita, KTH Royal Institute of Technology and Stockholm University, Roslagstullsbacken 23, SE-10691 Stockholm, Sweden*
[4]*Space Research Institute of the Russian Academy of Sciences, Profsoyuznaya Str. 84/32, Moscow 117997, Russia*

Accepted 2018 April 28. Received 2018 April 26; in original form 2017 December 15

ABSTRACT

We investigate the variability of optical and near-infrared light curves of the X-ray binary GX 339−4 on a time-scale of days. We use the data in four filters from six intervals corresponding to the soft state and from four intervals corresponding to the quiescent state. In the soft state, we find prominent oscillations with an average period $P = 1.772 \pm 0.003$ d, which is offset from the measured orbital period of the system by 0.7 per cent. We suggest that the measured periodicity originates from the superhumps. In line with this interpretation, we find no periodicity in the quiescent state. The obtained period excess ϵ is below typical values found for cataclysmic variables for the same mass ratio of the binary. We discuss the implications of this finding in the context of superhump theory.

Key words: accretion, accretion discs – black hole physics – X-rays: binaries.

1 INTRODUCTION

The spectral and variability properties of accreting black hole X-ray binaries have been studied since early 1960s. There are about 60 such sources known in our Galaxy, and every year there is, on average, one new discovered. The vast majority of these systems are transient low-mass X-ray binaries (LMXBs): they undergo an outburst and then return to quiescence on a time-scale of weeks to months. The recurrence time for most of the systems is comparable to, or larger than, the time-scale of the X-ray astronomy era, so most of the systems have been observed only once. A few persistent and recurrent systems have been identified, allowing a comparison of their properties between outbursts. The black hole binary GX 339−4 is among these systems.

The binary undergoes an outburst every 2–3 yeas and has been observed using multiwavelength campaigns (Smith et al. 1999; Homan et al. 2005; Cadolle Bel et al. 2011). GX 339−4 is the standard target for Small and Moderate Aperture Research Telescope System (SMARTS) monitoring and has been observed in the optical and near-infrared (ONIR) using this facility since 2002 (see Figs 1 a–d; Buxton et al. 2012). The long and frequent observations revealed the outbursts are proceeding through the sequence of flares, with the flares generally appearing before the transition to the soft state and after the reverse transition (Jain et al. 2001; Buxton & Bailyn 2004; Kalemci et al. 2013).

Such flares have also been detected in other sources and are believed to arise from the appearance of an additional component, probably of non-thermal origin (Callanan et al. 1995; Jain et al. 2001; Buxton & Bailyn 2004; Poutanen, Veledina & Revnivtsev 2014). On the other hand, the ONIR spectra during the soft state seem to approximately agree with the blackbody spectrum, suggesting a major contribution of the irradiated accretion disc. In the black hole binary XTE J1550−564, the soft-state evolution of the X-ray flux and ONIR magnitudes closely follow the exponential decay profile. By assuming that the ONIR radiation comes from the X-ray-heated accretion disc, it was possible to obtain the disc temperature using the relationship between the e-folding times in the X-ray and ONIR light curves (Poutanen et al. 2014), providing further grounds for considering ONIR emission as dominated by the disc. In the soft and intermediate states, the observed magnitudes tightly follow the blackbody track in the colour–magnitude diagram, with only marginal variations. In contrast, studies of SMARTS GX 339−4 light curves by Dinçer et al. (2012) revealed substantial variability around the mean in the soft state and, partially, during the flare, but not in the quiescent[1] state. The authors reported the period of soft-state variabilities to be equal to 1.77 d, which is close to the previously reported orbital period, $P_{\rm orb} \simeq 1.76$ d (see Hynes et al. 2003, Levine & Corbet 2006, and Heida et al. 2017 for a more recent estimate). Some interesting questions arise: which component in the binary system can produce variability at the orbital period and when can we observe such variations? Periodic variability can, in principle, come from the moving irradiated surface of the companion, or from the hotspot where the stream of matter from the

★ E-mail: ilia.kosenkov@utu.fi (IAK); alexandra.veledina@gmail.com (AV)

[1]The X-ray luminosity during the faintest episodes (Yen & Kong 2009) is within the luminosity range of the formal definition of the quiescent state (McClintock & Remillard 2006). We refer to these periods as quiescence throughout the paper.

companion hits the accretion disc, or be caused by the superhumps. To investigate these questions, we analysed the ONIR data from four outbursts of GX 339−4.

2 DATA SELECTION

We use the publicly available SMARTS data[2] described in Buxton et al. (2012). The source was observed in four ONIR bands, *V*, *I*, *J* and *H*, between MJD 52298 and MJD 55836. The observed magnitudes used in the present work are not corrected for extinction. We select intervals outside of the flares, when we expect the appearance of a non-thermal component. We exclude the interval MJD 52400–52550, because the observations are available in only one band (see Fig. 1). In addition, we separate intervals that show a difference in trend (such as around MJD 55400), thus ending up with six observational sets (OS1–6) in each of the four photometric filters (see the shaded areas in Fig. 1 a–d). The start and end MJD dates and the number of data points analysed in each filter of the selected intervals are given in Table 1.

The *Rossi X-ray Timing Explorer* All-Sky Monitor[3] (ASM) 3−5 keV light curve and 3−5 keV/1.5−3keV hardness ratios for the same dates are shown in Figs 1(e) and (f). In order to convert the observed count rate to the energy flux we adopt the procedure based on the assumption of the linear dependence of the energy flux in an ASM band on the count rates from all three ASM bands. We use the conversion coefficients calculated in Zdziarski et al. (2002). Although the selection is based on the optical data, the resulting intervals predominantly coincide with the source soft states, when we expect the dominant contribution of the accretion disc both in the ONIR and in the X-ray range.

3 DATA ANALYSIS AND RESULTS

In order to investigate the variability in different intervals and filters, we apply two techniques: a Bayesian analysis of periodicities (Section 3.1) and Lomb–Scargle periodograms (Section 3.2).

3.1 Bayesian inference

ONIR light curves show strong variability on a day time-scale. These fluctuations are complemented by the long-term trends that result from the variations on the outburst time-scale. We assume that the ONIR fluxes follow the model

$$F_j(t) \propto \exp\left(\psi_j t\right)\left[1+\Delta F_j \sin\left(\frac{2\pi}{P_j}t-\varphi_j\right)\right], \quad (1)$$

where j corresponds to the various filters (*V*, *I*, *J* or *H*), t is the time since the start of the fitted data set (in days), ψ_j is the decay rate, and ΔF_j, P_j and ϕ_j are the amplitudes, periods and phases of the most dominant modulation, respectively. The exponential factor is responsible for the trend in the data and was shown to give a good fit to similar data on XTE J1550−564 (Poutanen et al. 2014). The X-ray light curves are known to be described by the fast rise–exponential decay profile in the outburst (King & Ritter 1998), and hence our approximation of the ONIR light curve with the exponential decay profile implies an intrinsic connection between these energy ranges (e.g. if the disc is irradiated by the X-ray flux). We extend this model to the intervals where GX 339−4 becomes brighter by allowing the parameters ψ_j to be also positive (OS2, 5, 6).

We assume that the variability is caused by the geometrical properties of the source (e.g. varying inclination angle or projected area of the source, or the emission pattern). In this case, the variability amplitude is proportional to the source brightness; that is, it depends on the brightness multiplicatively. We show below that the amplitudes ΔF_j take similar values for different outbursts, suggesting a common origin of the variability source. If the variability are described by an additive model (i.e. the amplitude of variability is independent of flux), we expect variations in quiescence to have higher amplitude than in the soft state, which is not observed.

In order to simplify the fitting procedure and make the model under discussion suitable for fitting the observed data, we express the relationship in equation (1) in terms of magnitudes, keeping the first-order term of the sine component:

$$m_j(t) = m_j^0 + \mu_j t - \Delta m_j \sin\left(\frac{2\pi}{P_j}t-\varphi_j\right), \quad (2)$$

where $m_j(t)$ is the model magnitude, m_j^0 and μ_j account for the linear trend, and the last term comes from the first-order logarithm series expansion of the modulation component.

We use the Bayesian inference method to estimate the posterior distributions of each parameter. We search for periodicities close to the orbital period $P_{\rm orb} = 1.759$ d (Heida et al. 2017) and consider prior periods P_j in an interval of [1.6; 1.9] d. Other parameters are allowed to vary in a wide range: ϕ_j in $[-\pi; \pi]$ and Δm_j in [0; 0.5].

We process the light curves in each filter of each OS independently, meaning that we obtain 24 sets of parameters after fitting. The estimates of the model parameters are listed in Table 2. Systematically smaller observational errors in the *V* and *I* bands lead to smaller error bars for fitted parameters in these filters.[4]

In Fig. 2 we present the resulting parameters for the periodic component. The left panel shows the distribution of fitted periods and the right panel depicts the respective phases. In most cases, the estimates of the model parameters within one OS agree, within 1σ errors, in all four filters. However, the estimated values of P and ϕ in OS1 (*J* and *H*) and OS4 (*H*) are substantially different from the values obtained for other observational sets, because they are influenced by the large errors in observations and weak trends (see Fig. 1). In contrast, the P and ϕ values of the *V* and *I* bands tend to be consistent within one observation set. We also observe a significant evolution of periods from one OS to another, and the difference in periods exceeds the inferred errors.

OS2 is absent in Fig. 2 because the amplitudes obtained for OS2 are, on average, two times smaller than the amplitudes calculated for other observational sets, and the phases appear to be random (see Table 2). This indicates that there is no strong variability in the light curves of OS2. Further investigation (see Section 3.2) of the power spectral density (PSD) of the OS2 light curves supports this result. The PSDs also provide an explanation for the relatively small period errors obtained in OS2. The Bayesian inference method estimates the parameters of the most prominent modulation, which corresponds to the largest peak in the PSD within the allowed range of prior periods. In the case of OS2, there are many peaks of similar amplitude (see Fig. 7a). Because the peaks are quite narrow, the Bayesian fitting procedure estimates the parameters of these spuri-

[2] http://www.astro.yale.edu/buxton/GX339/
[3] http://xte.mit.edu/ASM_lc.html

[4] We note that the observations were carried out simultaneously in two filters, first in the *V* and *J* pair, then in *I* and *H* (Buxton et al. 2012); however, we neglect this difference and assume that all observations were simultaneous.

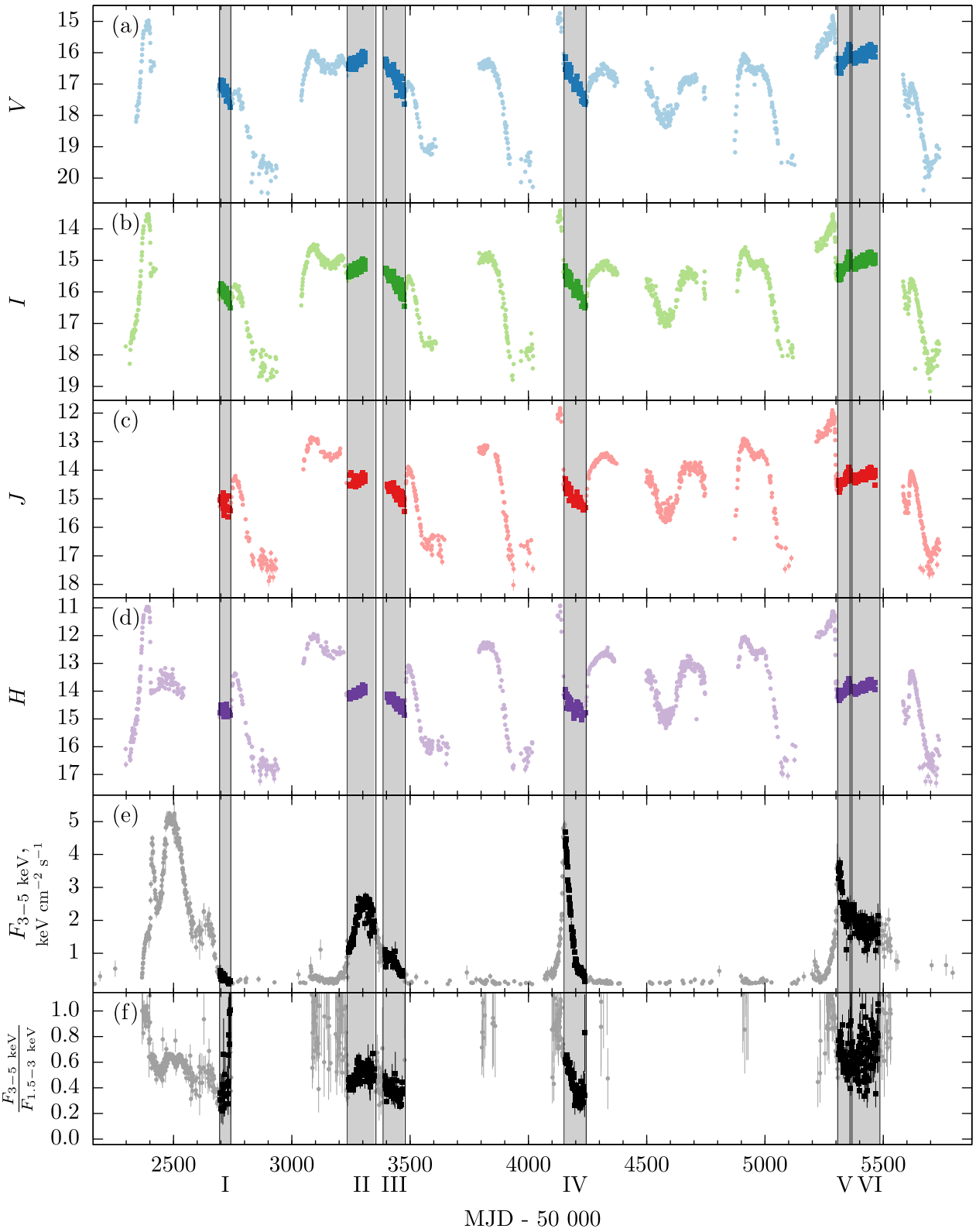

Figure 1. (a)–(d) ONIR light curves of GX 339−4 (the observed magnitudes) as reported in Buxton et al. (2012). The measurement errors are comparable to the symbol size. (e) *RXTE*/ASM B-band light curve. (f) ASM hardness ratio (ASM B/ASM A). Grey areas highlight the observation sets analysed in this work.

Table 1. List of start and end dates and the number of data points of the observational sets (OSs) analysed in this work.

OS	Start date	End date	Number of observations			
	MJD − 50000	MJD − 50000	*V*	*I*	*J*	*H*
1	2697.85	2738.83	34	35	31	30
2	3240.46	3310.49	53	56	24	21
3	3395.86	3474.86	57	55	56	55
4	4155.88	4239.80	56	60	47	43
5	5310.62	5360.61	48	45	42	48
6	5368.64	5466.50	66	66	60	53

ous peaks with reasonable precision. Even though the errors in the period values are small, the amplitudes of the modulations are at the level of error bars, which implies that the obtained periods cannot be trusted.

Examples of joint posterior distributions for periods and phases are shown in Fig. 3(a) (for the *V* band of OS1) and in Fig. 3(b) (for the *J* band of OS5). The contours are elongated along the direction of $P-\phi$ anti-correlation. This is a result of the model definition (see equation 2): setting the argument under the sine function to be constant, we obtain an anti-correlation of P and ϕ.

Examples of the observed and modelled light curves are shown in Fig. 4(a) (OS1, *V* filter) and Fig. 4(b) (OS5, *J* filter). The trend component (red dashed line), assumed to be linear in magnitudes, fits the long-term changes in brightness well. The modelled light curve (black solid line) tightly follows the data points, apart from several outliers. In the *V* band, the deviation of the data from the model is significant (more than 3σ), while in the *J* band the outliers are less than 2σ away from the model. The nature of the outliers is not clear.

We subtracted the fitted trends from the observed light curves and folded the resulting data points using best-fit estimated periods and phases. Examples of the folded light curves are presented in Figs 5(a)–(d) (OS1) and (e)–(h) (OS5). They allow us to investigate the profile of the detected periodic component and deviations from the simple sinusoidal shape. There is a hint of the secondary peak in all filters of OS5 near phase $\phi = 0.1$, but, owing to the large spread and small number of data points, we cannot draw any firm conclusion.

The detailed study of profile shape is complicated by the small number of data points: there are at most 60 data points per 100 d of observations (see Table 1). We study the effects of the non-sinusoidal profile on the estimated values of the period by introducing two additional harmonics to the model described in equation (2). We find that the new derived periods are within the errors of the ones estimated with one harmonic, and hence we see no evidence that the estimated periods are affected by the additional terms in the model. We also note that the PSDs obtained using Lomb-Scargle analysis clearly show (in the cases of a confident detection of variability) only one dominant periodic component, and the value of the period at which the PSD reaches maximum agrees with the respective value obtained using Bayesian inference.

We calculated the weighted mean period for light curves of OS1, 3, 4, 5 and 6, and obtained $P = 1.772$ d (standard deviation 0.003 d). The weights, chosen to be inversely proportional to the variances of period posterior distributions, allowed us to reduce the contribution of parameters with poor estimates, such as the ones obtained for the *J* and *H* bands of OS1. However, the weighted average value differs significantly from the orbital periods proposed previously, $P_{\rm orb} = 1.7557 \pm 0.0004$ d (Hynes et al. 2003; Levine & Corbet 2006) and $P_{\rm orb} = 1.7587 \pm 0.0005$ d (Heida et al. 2017). This difference cannot be explained by the measurement errors, as the values of both orbital periods and the periods found in our work are obtained with high precision, the latter thanks to the long duration of the observations. The first spectroscopic orbital period was obtained using data taken during the 2002 outburst (Hynes et al. 2003), about half a year before our OS1. More recently, the orbital period was measured during the quiescent state (Heida et al. 2017), almost five years after the last data set analysed in this work was observed.

3.2 Lomb–Scargle analysis of ONIR light curves

An alternative method to investigate the periodic components present in the observed light curves is to apply spectral analysis. We use the Lomb–Scargle method (Scargle 1982) to study the soft-state observations (OS1 to 6), as well as a number of intervals during the quiescent state. Unlike the direct fitting of one harmonic, which allows only the most prominent variable component to be detected, spectral analysis can uncover multiple periodic components of different amplitudes (if present).

In order to apply the Lomb–Scargle method to the observed light curves, we first subtract trends. We adopt the trend model similar to the one discussed in Section 3.1. Preserving the notation introduced in equation (2), the trend can be approximated as follows:

$$\hat{m}_j^{\rm mdl}(t) = \hat{m}_j^0 + \hat{\mu}_j t, \tag{3}$$

where $\hat{m}_j^{\rm mdl}$ are model magnitudes, and $\hat{m}_j^0$ and $\hat{\mu}_j$ are linear trend parameters. The resulting coefficients can be found in Table 3. After removal of the linear trend, we applied the spectral analysis procedure to the residuals.

Most of the light curves have only one data point per night, with rare exceptions of two subsequent observations in one night. For strictly periodic observations (uniform time series) with a time step of 1 d, the highest (Nyquist) frequency is $0.5\,{\rm d}^{-1}$, corresponding to the smallest period of 2 d. However, the analysed time series are not strictly uniform, because the time interval between two subsequent observations is not precisely equal to 1 d. Instead, a typical interval ranges from 0.95 to 1.05 d, making light curves quasi-uniform time series with irregular gaps. As a result, we expect that a periodic modulation with $P \approx 1.77$ d will produce a peak in the PSD at frequency $\nu_1 = 0.565\,{\rm d}^{-1}$ and an alias at frequency $\nu_2 = 0.435\,{\rm d}^{-1}$, which corresponds to a period of $\sim$2.29 d. The relative amplitudes of these peaks depend on the profile of the window function, which in turn depends on the distribution of observation times within the studied time interval and on the number of observations. In general, for a non-uniform time series, the amplitude of the true signal is expected to be larger than the amplitudes of its aliases. We verifiy this property by studying the individual window function in each case.

In order to distinguish between spurious and real peaks, we estimate the false alarm probabilities (FAPs) of the highest detected peak in each PSD. The FAP can be obtained from the cumulative probability distribution (CDF) of maxima of Lomb–Scargle PSDs, calculated for the time series with no periodic component. A number of analytical formulae describing CDFs were derived for uniform series (see e.g. Scargle 1982), but no simple analytical solution was found for a general non-uniform series, and CDFs are usually constructed using numerical simulations. In order to estimate the FAP of signals detected in the PSDs of GX 339−4, we adopt the numerical scheme described in Frescura, Engelbrecht

Table 2. Values of model parameters estimated using Bayesian inference. The parameters m_j^0 and μ_j determine the linear trend, and Δm_j, P_j and ϕ_j are the amplitudes, periods and phases of the periodic component, respectively. The errors correspond to 1σ.

	Model parameters				
Band	m_j^0	$\mu_j \times 10^{-2}$ [d^{-1}]	Δm_j	P_j [d]	ϕ_j [rad]
			OS 1		
V	16.972 ± 0.001	1.334 ± 0.001	0.135 ± 0.003	1.767 ± 0.001	0.668 ± 0.031
I	15.829 ± 0.001	1.239 ± 0.001	0.103 ± 0.003	1.768 ± 0.001	0.749 ± 0.044
J	14.974 ± 0.001	0.878 ± 0.001	0.122 ± 0.008	1.756 ± 0.003	0.865 ± 0.133
H	14.620 ± 0.001	0.614 ± 0.001	0.090 ± 0.008	1.746 ± 0.005	1.434 ± 0.212
			OS 2		
V	16.452 ± 0.001	−0.477 ± 0.001	0.050 ± 0.002	1.608 ± 0.001	−0.299 ± 0.071
I	15.439 ± 0.001	−0.461 ± 0.001	0.065 ± 0.002	1.744 ± 0.001	−2.562 ± 0.048
J	14.288 ± 0.001	−0.050 ± 0.001	0.095 ± 0.008	1.840 ± 0.001	−3.075 ± 0.061
H	14.172 ± 0.001	−0.307 ± 0.001	0.059 ± 0.008	1.778 ± 0.002	2.985 ± 0.128
			OS 3		
V	16.322 ± 0.001	1.151 ± 0.001	0.124 ± 0.002	1.776 ± 0.001	−1.372 ± 0.043
I	15.288 ± 0.001	0.987 ± 0.001	0.136 ± 0.002	1.776 ± 0.001	−1.550 ± 0.037
J	14.405 ± 0.001	0.838 ± 0.001	0.123 ± 0.006	1.777 ± 0.001	−1.597 ± 0.142
H	14.081 ± 0.001	0.705 ± 0.001	0.109 ± 0.005	1.777 ± 0.001	−1.680 ± 0.132
			OS 4		
V	16.393 ± 0.001	1.344 ± 0.001	0.129 ± 0.002	1.769 ± 0.001	−1.413 ± 0.024
I	15.400 ± 0.001	1.129 ± 0.001	0.128 ± 0.002	1.770 ± 0.001	−1.480 ± 0.025
J	14.599 ± 0.001	0.883 ± 0.001	0.091 ± 0.006	1.768 ± 0.002	−1.688 ± 0.136
H	14.188 ± 0.001	0.910 ± 0.001	0.127 ± 0.006	1.757 ± 0.001	−0.860 ± 0.091
			OS 5		
V	16.500 ± 0.001	−1.171 ± 0.001	0.152 ± 0.002	1.774 ± 0.001	−0.298 ± 0.029
I	15.473 ± 0.001	−1.157 ± 0.001	0.135 ± 0.002	1.773 ± 0.001	−0.187 ± 0.032
J	14.554 ± 0.001	−1.015 ± 0.001	0.142 ± 0.006	1.774 ± 0.001	−0.158 ± 0.099
H	14.190 ± 0.001	−0.959 ± 0.001	0.133 ± 0.004	1.775 ± 0.001	−0.350 ± 0.063
			OS 6		
V	16.163 ± 0.001	−0.242 ± 0.001	0.114 ± 0.002	1.771 ± 0.001	0.177 ± 0.033
I	15.130 ± 0.001	−0.236 ± 0.001	0.107 ± 0.002	1.770 ± 0.001	0.356 ± 0.035
J	14.290 ± 0.001	−0.243 ± 0.001	0.092 ± 0.004	1.768 ± 0.001	0.836 ± 0.110
H	13.949 ± 0.001	−0.225 ± 0.001	0.090 ± 0.004	1.776 ± 0.001	0.061 ± 0.109

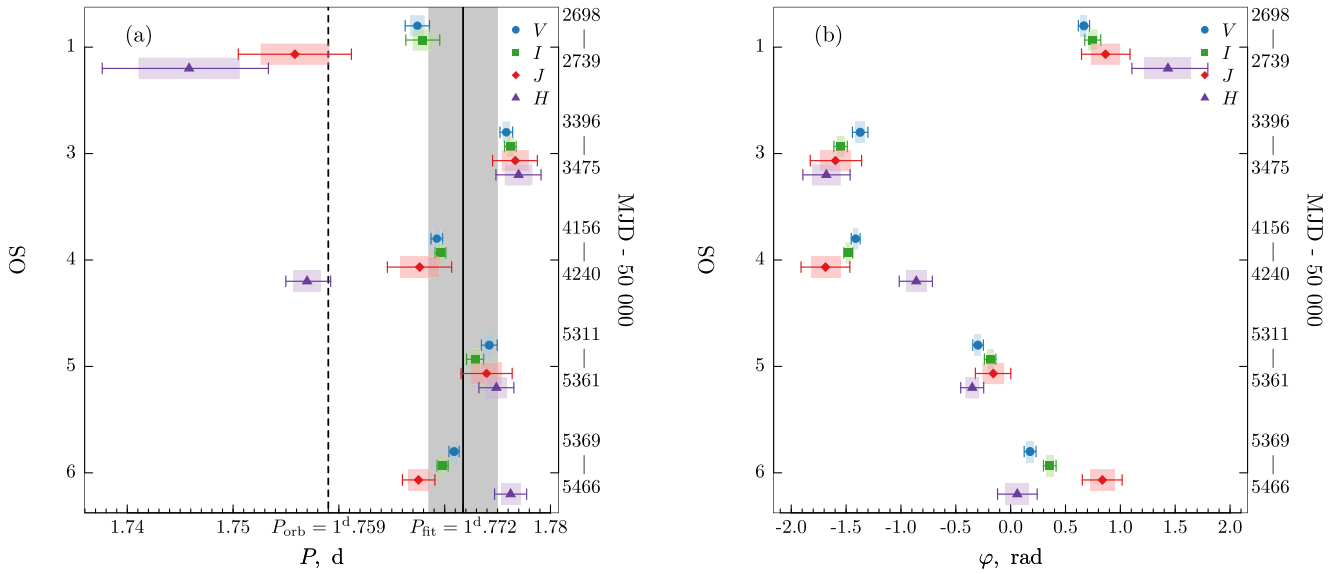

Figure 2. (a) Distribution of the periods obtained for five intervals using Bayesian inference. The vertical solid line denotes the weighted mean of all shown periods; the grey area indicates the standard deviation of the period distribution. The vertical dashed line marks the orbital period of the binary (estimated in Heida et al. 2017). (b) Distribution of the obtained phases. The shaded areas and horizontal bars correspond to 1σ and 2σ errors, respectively.

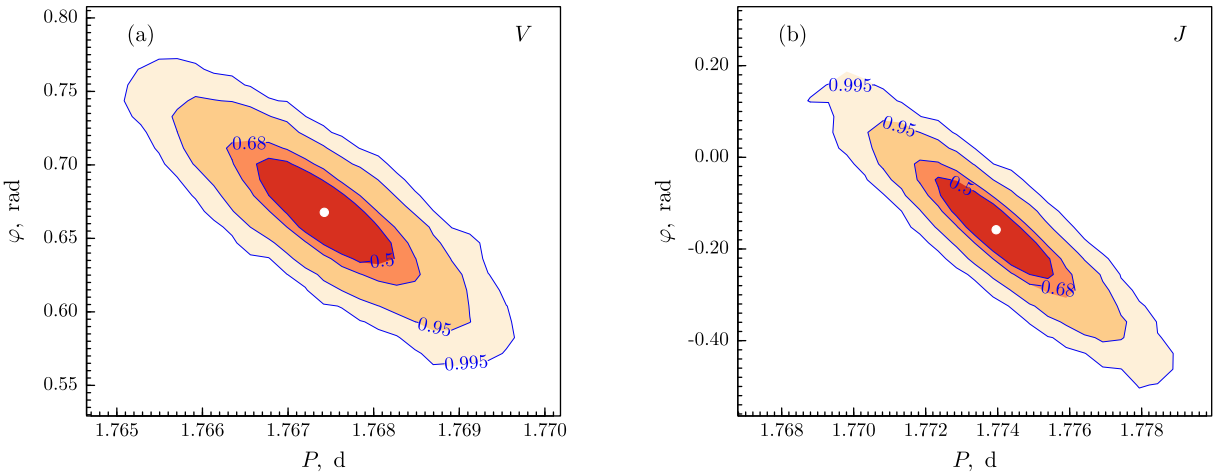

Figure 3. (a) Joint posterior distributions of the period (P) and phase (ϕ), obtained for the V band of OS1. (b) Joint posterior distributions obtained for the J band of OS5. Contours represent the 0.5, 0.68, 0.95 and 0.995 credibility levels.

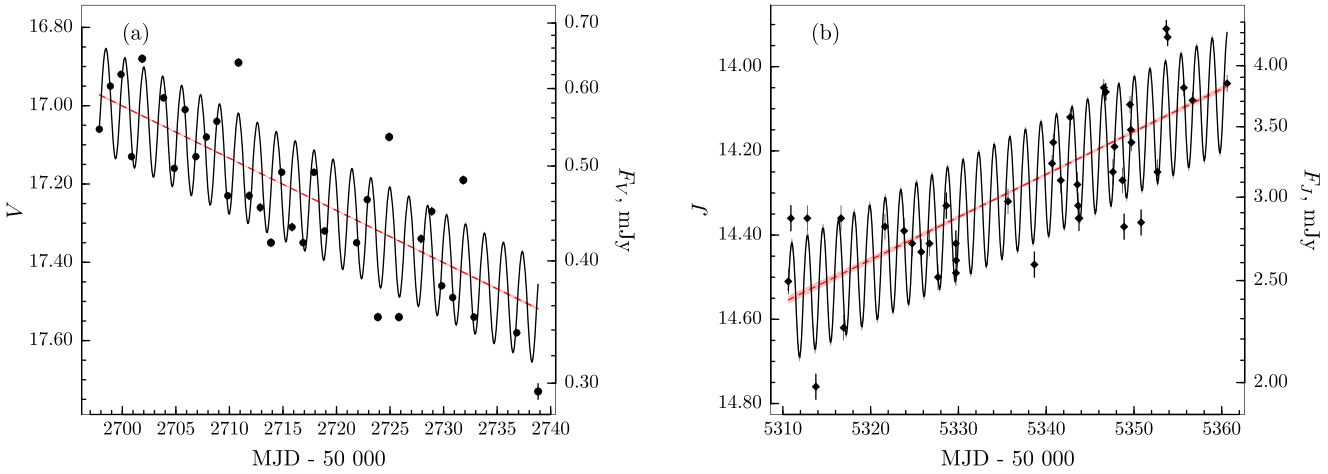

Figure 4. The observed light curves in (a) the V band of OS1 and (b) the J band of OS5. The trend components are shown with the red dashed lines, and the total model is shown with the black solid line. Errors are 1σ; error bars are comparable to the symbol size.

& Frank (2008). This method involves simulating a large number of test (random) time series with the same window function, and calculating the maxima of the corresponding PSDs. The obtained values are then used to construct an approximation of the CDF, which in turn provides an estimate of the FAP for the maximum peak in the PSD of the observed time series. After some investigation, we decided to limit the number of test time series to 10^4 for each band of each observation interval. The resulting FAPs, amplitudes of the maximum peak in the PSDs and corresponding periods are presented in Table 3. We note that the FAPs are calculated for each light curve independently, not taking into account the probability of detecting the peak at a particular frequency in each light curve.

Fig. 6 shows typical PSDs obtained for the V band of OS1 (panel a) and the J band of OS5 (panel b). Two clearly distinguishable peaks can be seen in each panel. The highest peak in these two cases ($\nu \approx 0.56\,\mathrm{d}^{-1}$, or $P \approx 1.77$ d) corresponds to the actual short-term variability found in the observed light curves of GX 339−4, while the other one ($\nu \approx 0.44\,\mathrm{d}^{-1}$, $P \approx 2.28$ d) is caused by aliasing. The relative amplitudes of the signal peak and its alias differ between OSs and bands, depending on the data spread and on the number of data points. The FAPs of the highest peaks of the PSDs in Fig. 6 are 10.4 and 0.1 per cent, respectively, indicating that in the V band of OS1 the periodic component is present, but that there is a high probability of this peak being caused by a coincidence, while for the J band of OS5, it is highly unlikely that the observed peak is spurious. PSDs of other OSs resemble those shown in Fig. 6, with the one exception of OS2 (see Fig. 7a). Both the Bayesian fitting procedure and the Lomb–Scargle method failed to detect any significant periodic component, with period close to the orbital period, in all ONIR bands of OS2.

An atypical PSD shape was obtained for OS4 (see Fig. 7b). The highest peak is found at the alias frequency ($\nu \approx 0.44\,\mathrm{d}^{-1}$), although the peak at the true frequency is only slightly lower. The FAPs of these peaks in the V and I bands (see Table 3) are low, indicating that the observed light curves indeed contain periodic components. However, the FAP calculated for the J and H bands are relatively high, which in turn means that the periodic component in these two bands cannot be reliably identified. Although the highest peak is found at the alias frequency, it can still be used to estimate

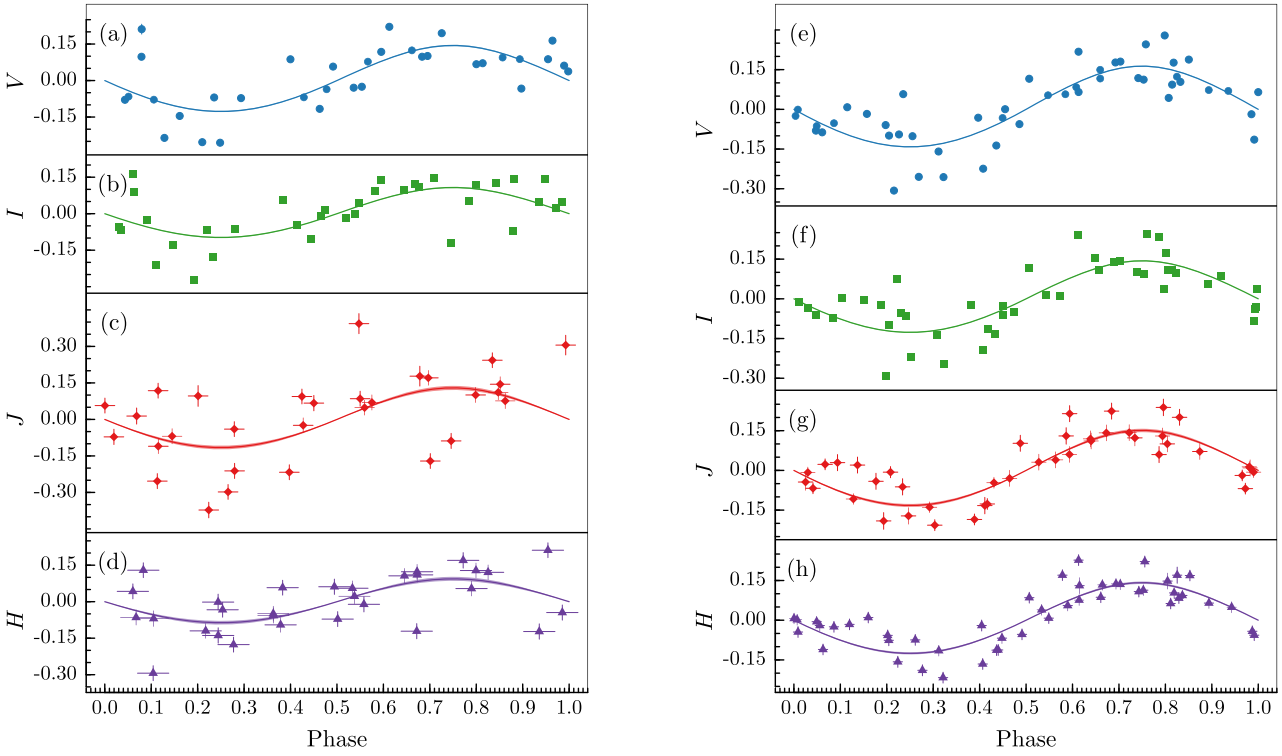

Figure 5. Folded light curves with trend subtracted: (a)–(d) OS1; (e)–(h) OS5. Horizontal error bars correspond to errors in phase, which are caused by the uncertainties in the estimated model period and phase values.

the properties of the periodic component, at least in the V and I bands.

4 DISCUSSION

In order to investigate the origin of the reported variability, we apply Lomb–Scargle spectral analysis to the data in the quiescent state. The observed flux of GX 339−4 during its faintest flux periods was contaminated by the flux from nearby field stars (Buxton et al. 2012). These observations are included in the publicly available SMARTS data, but we did not use these data in our analysis. The dates for the selected intervals are listed in Table 4. We found that the FAPs of the highest PSD peaks range from 30 to 90 per cent, and the corresponding frequencies of the peaks appear to be random.

The contribution of the secondary to the total NIR flux is estimated to reach 50 per cent in quiescence (Heida et al. 2017), and hence the donor star contributes ∼5 per cent during soft states, when the total NIR luminosity is about an order of magnitude larger. However, the X-rays originating from the vicinity of the compact object can irradiate the surface of the donor star and increase its contribution to the total flux in the soft state. We estimate this contribution by considering the X-ray luminosity to be 10 per cent of the Eddington limit for a 5 $M_\odot$ black hole (Hynes et al. 2003; Heida et al. 2017), and by assuming the X-ray emission pattern to follow Lambert's law (proportional to the cosine of the inclination angle between the direction of outgoing emission and the disc axis; see, however, a more precise approximation in Suleimanov, Lipunova & Shakura 2008). The disc covers a fraction of the secondary surface, its opening angle is assumed to be 12° (de Jong, van Paradijs & Augusteijn 1996), and the binary mass ratio is 0.18 (Heida et al. 2017). We take the distance to the source to be equal to 10 kpc (Hynes et al. 2003; Heida et al. 2017) and the interstellar reddening to be $A_V = 3.7$ (Zdziarski et al. 1998; Buxton et al. 2012). We obtain the flux from the irradiated surface of the donor to be of the order of 0.01 mJy in the V band, much smaller than the observed flux of ∼0.5 mJy from the source in the soft state. We conclude that the soft-state emission is dominated by the accretion disc, which is also responsible for the observed variability.

The small (about 1 per cent) excess above the orbital period and the absence of oscillations during quiescence suggest that the observed variability is caused by the superhumps. Superhumps are optical periodic modulations that were originally observed in SU UMa dwarf novae (Vogt 1974; Warner 1975). Superhumps usually accompany super-outbursts and are never observed during normal outbursts or quiescent states of dwarf novae (Osaki 1996). These modulations are believed to be caused by the slow precession of an eccentric accretion disc, which is deformed owing to the presence of the 3:1 resonance within it (Whitehurst & King 1991). The prograde precession of the disc leads to the observed superhump period, $P_{\rm sh}$, which is slightly larger (by a few per cent) than the orbital period, while a more rare retrograde precession causes the observed superhump period to be smaller (Wood et al. 2011). The actual period of the disc precession is usually much longer than the orbital period, and can be expressed as $P_{\rm prec} = P_{\rm sh}/\epsilon$, where $\epsilon = (P_{\rm sh} - P_{\rm orb})/P_{\rm orb}$ is the superhump period excess (Haswell et al. 2001). The period excess can in turn be expressed as (Osaki 1985; Mineshige, Hirose & Osaki 1992)

$$\epsilon = \frac{1}{4}\frac{q}{\sqrt{1+q}}\eta^{\frac{3}{2}}, \quad (4)$$

where $q = M_2/M_1$ is the mass ratio and $\eta = R_{\rm d}/R_{\rm crit}$ is the ratio of the disc radius to the critical radius, beyond which the disc becomes unstable (Hirose & Osaki 1990).

Table 3. Fitted trend parameters ($\hat{m}_j^0$ and $\hat{\mu}_j$, errors are 1σ), values of the highest peak in the power spectral density (PSD), corresponding periods (P_j) and false alarm probabilities (FAPs) of these highest peaks.

	Spectral analysis parameters				
Band	$\hat{m}_j^0$	$\hat{\mu}_j \times 10^{-2}$ [d^{-1}]	max (PSD)	P_j [d]	FAP [per cent]
			OS 1		
V	16.965 ± 0.001	1.429 ± 0.001	0.114	1.77	10.35
I	15.834 ± 0.001	1.262 ± 0.001	0.072	1.77	26.89
J	15.015 ± 0.001	0.685 ± 0.001	0.145	1.76	71.21
H	14.639 ± 0.001	0.493 ± 0.001	0.059	1.74	57.46
			OS 2		
V	16.456 ± 0.001	-0.474 ± 0.001	0.054	1.72	76.21
I	15.431 ± 0.001	-0.446 ± 0.001	0.048	1.75	79.91
J	14.302 ± 0.001	-0.067 ± 0.001	0.188	1.50	13.97
H	14.154 ± 0.001	-0.287 ± 0.001	0.053	7.87	63.30
			OS 3		
V	16.316 ± 0.001	1.178 ± 0.001	0.245	1.78	8.40
I	15.291 ± 0.001	1.006 ± 0.001	0.260	1.78	0.93
J	14.415 ± 0.001	0.830 ± 0.001	0.252	1.78	0.11
H	14.074 ± 0.001	0.719 ± 0.001	0.178	1.78	0.23
			OS 4		
V	16.387 ± 0.001	1.376 ± 0.001	0.268	2.30	0.31
I	15.392 ± 0.001	1.159 ± 0.001	0.288	2.30	0.20
J	14.606 ± 0.001	0.871 ± 0.001	0.119	2.30	35.63
H	14.199 ± 0.001	0.880 ± 0.001	0.170	2.32	44.58
			OS 5		
V	16.507 ± 0.001	-1.141 ± 0.001	0.295	1.77	0.03
I	15.469 ± 0.001	-1.113 ± 0.001	0.225	1.77	0.11
J	14.571 ± 0.001	-1.099 ± 0.001	0.200	1.78	0.11
H	14.182 ± 0.001	-0.871 ± 0.001	0.202	1.77	0.06
			OS 6		
V	16.179 ± 0.001	-0.269 ± 0.001	0.214	1.77	0.03
I	15.144 ± 0.001	-0.262 ± 0.001	0.189	1.77	0.05
J	14.273 ± 0.001	-0.218 ± 0.001	0.132	1.78	1.45
H	13.963 ± 0.001	-0.245 ± 0.001	0.111	1.78	0.47

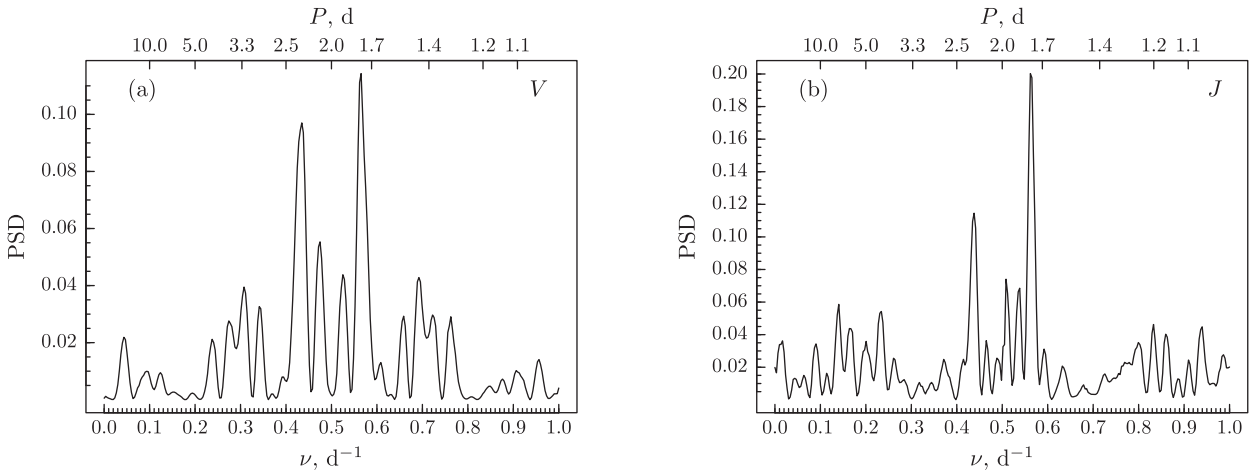

Figure 6. Example power spectral densities calculated for (a) the *V* band of OS1 and (b) the *J* band of OS5. The values of the highest peaks, corresponding periods and false alarm probabilities are given in Table 3.

Superhumps have also been detected in black hole transient LMXBs (Kato, Mineshige & Hirata 1995; O'Donoghue & Charles 1996; Uemura et al. 2000; Zurita et al. 2002, 2008). One of the most plausible explanations of LMXB superhumps is that changes in both the area of the disc visible to the observer and the modulation of the fraction of intercepted X-ray emission over the superhump cycle contribute to the observed optical modulations (Haswell et al. 2001). The 3:1 resonance condition restricts the mass ratio to $q \leq 0.25$ (Whitehurst & King 1991) for the systems demonstrating superhump modulations. The condition is typically fulfilled in

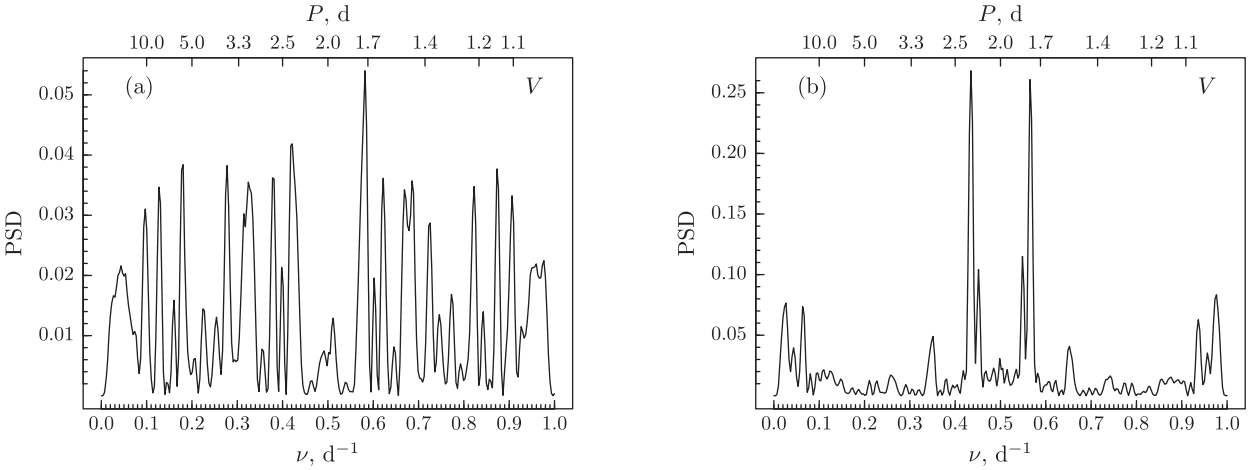

Figure 7. Examples of atypical profiles of power spectral densities (PSDs). (a) PSD calculated for the *V* band of OS2. The highest peak could be spurious, which is indicated by the high false alarm probability of 76 per cent (see Table 3). (b) PSD of the *V* band of OS4. The alias peak is higher than the real peak, unlike in other OSs.

Table 4. List of start and end dates, the number of observations, and the average magnitudes with standard deviations for the analysed quiescent states.

Start date	End date	No. of observations				Average magnitude			
MJD − 50000	MJD − 50000	*V*	*I*	*J*	*H*	*V*	*I*	*J*	*H*
2856.60	2943.50	31	27	33	41	19.65 ± 0.06	18.31 ± 0.03	17.24 ± 0.12	16.67 ± 0.07
3560.70	3660.50	20	22	27	33	18.94 ± 0.12	17.63 ± 0.01	16.54 ± 0.02	15.96 ± 0.02
3968.59	4019.51	13	17	9	14	19.44 ± 0.04	17.85 ± 0.07	16.71 ± 0.04	16.17 ± 0.15
5700.62	5735.62	18	20	19	20	19.36 ± 0.20	18.03 ± 0.21	16.82 ± 0.17	16.31 ± 0.28

LMXBs with massive primaries (Casares & Jonker 2014), and is also true for GX 339−4, for which $q = 0.18 \pm 0.05$ was recently measured (Heida et al. 2017). We estimated a superhump period excess for GX 339−4 of $\epsilon = 0.007 \pm 0.002$, which is smaller than the typical values obtained for cataclysmic variables with the same mass ratio (see Fig. 8 and Smith et al. 2007). For this ϵ, the disc precession period of GX 339−4 is $P_{\rm prec} = 240$ d.

In Fig. 8 we show that the analytical $\epsilon - q$ relationship (equation 4, solid black line) aligns well with the observed dwarf novae if we put $\eta \approx 0.9$, but LMXBs tend to have smaller superhump period excesses. Smaller values of η could potentially account for this discrepancy. In order to explain the superhump excess observed in GX 339−4, $\eta = 0.1$ is required. The physical reasons for the accretion disc in GX 339−4 being substantially smaller are not clear.

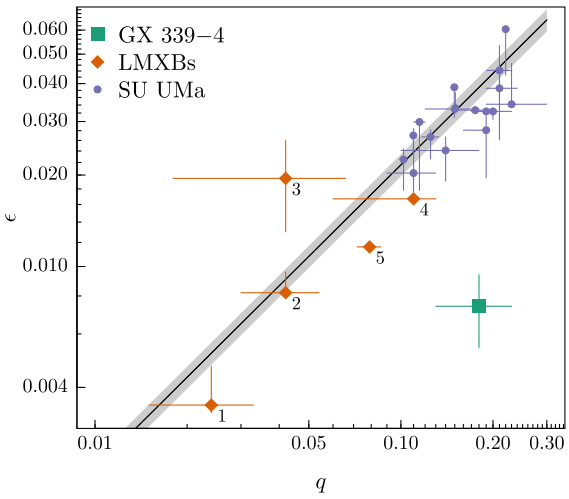

Figure 8. Period excess of superhumps as a function of the mass ratio. Data are adopted from Smith et al. (2007) (see their table 5 and references therein). Binary mass ratios of LMXBs are taken from Casares & Jonker (2014) (see their table 1 and references therein) and Wu et al. (2015) for N Mus 1991. Errors are 1σ. The labelled LMXBs are: (1) KV UMa (XTE J1118+480), (2) Qz Vul (GS 2000+2), (3) V1482 Aqr (GRS 1915+105), (4) V518 Per (GRO J0422+32), (5) GU Mus (N Mus 1991).

5 CONCLUSIONS

We investigated the variability of the long-term *V*, *I*, *J* and *H* light curves at periods close to the orbital period. We chose six intervals of observations away from the flares, which coincide with the soft state of the source. We used two methods, namely Bayesian inference and Lomb–Scargle spectral analysis, and found prominent oscillations in five intervals (OS1, 3, 4, 5 and 6) at $P \approx 1.772$ d, while the spread in the data points of OS2 does not allow reliable estimation of the periodic oscillations. We additionally considered four intervals corresponding to the quiescent state and found that none of these light curves demonstrates significant oscillations. We conclude that the observed oscillations appear during the soft states and probably originate from the accretion disc.

The calculated periods indicate, despite the long time gaps between subsequent soft states, that the detected period is fairly stable (Fig. 2, left panel). The spread of periods in different filters within one OS is typically much smaller than the spread of periods for different OSs.

Despite the spread of the periods in the soft-state data, the determined periods (those with small error bars, e.g. in the *V* and *I* filters) are systematically larger than the values obtained for the orbital period of the system, 1.7557 ± 0.0004 d (Hynes et al. 2003) and 1.7587 ± 0.0005 d (Heida et al. 2017). We obtained the average period of $P = 1.772$ d (see Fig. 2, solid black line) and the standard deviation of the period distribution is 0.003 d for the five observational sets with the prominent periodic component. The difference between the orbital period and the measured periods significantly exceeds typical measurement errors in 17 out of 20 cases. Such high accuracy in period estimation was only possible thanks to the exceptionally long observations of the system, despite the small number of points in each period. We compared the superhump excess period to other systems, LMXBs and SU UMa dwarf novae, and found that the excess in GX 339−4 is substantially below that expected for a binary with the same mass ratio. The physical reasons for this are, however, not clear.

ACKNOWLEDGEMENTS

This paper has made use of SMARTS optical/near-infrared light curves that are available at www.astro.yale.edu/smarts/xrb/home.php. IK acknowledges the Nordita Visiting PhD Fellow Program. AV acknowledges support from the Academy of Finland, grant 309308, and the Ministry of Education and Science of the Russian Federation, grant 14.W03.31.0021. We thank Juri Poutanen, Vitaly Neustroev, Valery Suleimanov and Emrah Kalemci for helpful discussions and Jorge Casares, Tolga Dinçer and the referee for comments that greatly improved the manuscript.

REFERENCES

Buxton M. M., Bailyn C. D., 2004, ApJ, 615, 880
Buxton M. M., Bailyn C. D., Capelo H. L., Chatterjee R., Dinçer T., Kalemci E., Tomsick J. A., 2012, AJ, 143, 130
Cadolle Bel M. et al., 2011, A&A, 534, A119
Callanan P. J. et al., 1995, ApJ, 441, 786
Casares J., Jonker P. G., 2014, Space Sci. Rev., 183, 223
de Jong J. A., van Paradijs J., Augusteijn T., 1996, A&A, 314, 484
Dinçer T., Kalemci E., Buxton M. M., Bailyn C. D., Tomsick J. A., Corbel S., 2012, ApJ, 753, 55
Frescura F. A. M., Engelbrecht C. A., Frank B. S., 2008, MNRAS, 388, 1693
Haswell C. A., King A. R., Murray J. R., Charles P. A., 2001, MNRAS, 321, 475
Heida M., Jonker P. G., Torres M. A. P., Chiavassa A., 2017, ApJ, 846, 132
Hirose M., Osaki Y., 1990, PASJ, 42, 135
Homan J., Buxton M., Markoff S., Bailyn C. D., Nespoli E., Belloni T., 2005, ApJ, 624, 295
Steeghs D., Casares J., Charles P. A., O'Brien K., 2003, ApJL, 583, L95
Jain R. K., Bailyn C. D., Orosz J. A., McClintock J. E., Remillard R. A., 2001, ApJ, 554, L181
Kalemci E., Dinçer T., Tomsick J. A., Buxton M. M., Bailyn C. D., Chun Y. Y., 2013, ApJ, 779, 95
Kato T., Mineshige S., Hirata R., 1995, PASJ, 47, 31
King A. R., Ritter H., 1998, MNRAS, 293, L42
Levine A. M., Corbet R., 2006, Astron. Telegram, 940
McClintock J. E., Remillard R. A., 2006, Black Hole Binaries, Cambridge University Press, Cambridge, UK. p. 157
Mineshige S., Hirose M., Osaki Y., 1992, PASJ, 44, L15
Osaki Y., 1985, A&A, 144, 369
Osaki Y., 1996, PASP, 108, 39
O'Donoghue D., Charles P. A., 1996, MNRAS, 282, 191
Poutanen J., Veledina A., Revnivtsev M. G., 2014, MNRAS, 445, 3987
Scargle J. D., 1982, ApJ, 263, 835
Smith A. J., Haswell C. A., Murray J. R., Truss M. R., Foulkes S. B., 2007, MNRAS, 378, 785
Smith I. A. et al., 1999, ApJ, 519, 762
Suleimanov V. F., Lipunova G. V., Shakura N. I., 2008, A&A, 491, 267
Uemura M. et al., 2000, PASJ, 52, L9
Vogt N., 1974, A&A, 36, 369
Warner B., 1975, MNRAS, 170, 219
Whitehurst R., King A., 1991, MNRAS, 249, 25
Wood M. A., Still M. D., Howell S. B., Cannizzo J. K., Smale A. P., 2011, ApJ, 741, 105
Wu J. et al., 2015, ApJ, 806, 92
Yen T.-C., Kong A. K. H., 2009, Astron. Telegram, 2281
Zdziarski A. A., Poutanen J., Mikolajewska J., Gierlinski M., Ebisawa K., Johnson W. N., 1998, MNRAS, 301, 435
Zdziarski A. A., Poutanen J., Paciesas W. S., Wen L., 2002, ApJ, 578, 357
Zurita C., Durant M., Torres M. A. P., Shahbaz T., Casares J., Steeghs D., 2008, ApJ, 681, 1458
Zurita C. et al., 2002, MNRAS, 333, 791

This paper has been typeset from a TEX/LATEX file prepared by the author.